

See discussions, stats, and author profiles for this publication at: <https://www.researchgate.net/publication/266388122>

Facile Fabrication of WO₃ Nanoplates Thin Films with Dominant Crystal Facet of (002) for Water Splitting

ARTICLE in CRYSTAL GROWTH & DESIGN · OCTOBER 2014

Impact Factor: 4.89 · DOI: 10.1021/cg5012154

CITATIONS

12

READS

226

9 AUTHORS, INCLUDING:



Jin You Zheng

Sogang University

15 PUBLICATIONS 101 CITATIONS

[SEE PROFILE](#)



Van Thanh-Khue

Industrial University of Ho Chi Minh

9 PUBLICATIONS 61 CITATIONS

[SEE PROFILE](#)



Zeeshan Haider

Sogang University

5 PUBLICATIONS 26 CITATIONS

[SEE PROFILE](#)

Facile Fabrication of WO_3 Nanoplates Thin Films with Dominant Crystal Facet of (002) for Water Splitting

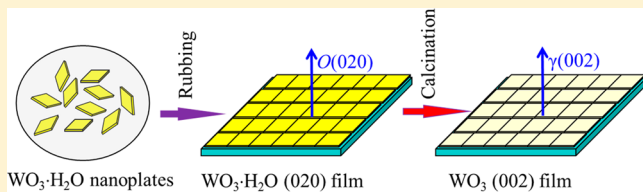
Jin You Zheng,[†] Guang Song,[†] Jisang Hong,[#] Thanh Khue Van,[†] Amol Uttam Pawar,[†] Do Yoon Kim,[†] Chang Woo Kim,[†] Zeeshan Haider,[†] and Young Soo Kang*,[†]

[†]Korea Center for Artificial Photosynthesis, Department of Chemistry, Sogang University, Seoul 121-742, South Korea

[#]Department of Physics, Pukyong National University, Busan 608-737, South Korea

Supporting Information

ABSTRACT: Single crystalline orthorhombic phase tungsten trioxide monohydrate ($\text{O-WO}_3\cdot\text{H}_2\text{O}$, space group: $Pmn\bar{b}$) nanoplates with a clear morphology and uniform size distribution have been synthesized by the hydrothermal method and fabricated on the surface of fluorine doped tin oxide (FTO) coated glass substrates with selective exposure of the crystal facet by the finger rubbing method. The rubbing method can easily arrange the $\text{O-WO}_3\cdot\text{H}_2\text{O}$ nanoplates along the (020) facet on the FTO substrate. The $\text{O-WO}_3\cdot\text{H}_2\text{O}$ nanoplate can be converted to monoclinic phase WO_3 ($\gamma\text{-WO}_3$, space group: $P21/n$) with dominant crystal facet of (002) without destroying the plate structure. Crystal morphologies, structures, and components of the powders and films have been determined by scanning electron microscopy, transmission electron microscopy, X-ray diffraction, Raman, X-ray photoelectron spectroscopy, etc. The band gap energies of the $\text{O-WO}_3\cdot\text{H}_2\text{O}$ and $\gamma\text{-WO}_3$ nanoplates were determined as ca. 2.26 and 2.49 eV, respectively. Photoelectrochemical properties of the films with (002) dominant crystal facet have also been checked for discussion of further application in water oxidation. The advantage of (002) facet dominant film was investigated by comparing to one spin-coated $\gamma\text{-WO}_3$ thin film with the same thickness via photoelectrochemical characterizations such as photocurrent, incident photon to current efficiency, and electrochemical impedance spectroscopy.



1. INTRODUCTION

WO_3 has many potential applications in electrochromic devices,^{1,2} gas sensors,³ photocatalytic systems,⁴ and photo-electrochemical (PEC) water splitting.⁵ For PEC water splitting, mainly n-type semiconductors such as TiO_2 ,⁶ ZnO ,⁷ $\alpha\text{-Fe}_2\text{O}_3$,⁸ BiVO_4 ,⁹ and WO_3 ^{5,10} are very popular. Among them, WO_3 is a very important $5d^0$ transition metal oxide with a smaller band gap (~2.8 eV) than that of other semiconductors such as TiO_2 (~3.2 eV) and ZnO (~3.2 eV). This results in the absorption of solar light in the visible range. WO_3 crystals show five phase transitions in the temperature range of -180 to 900 °C changing from tetragonal ($\alpha\text{-WO}_3$, > 740 °C) → orthorhombic ($\beta\text{-WO}_3$, 330–740 °C) → monoclinic I ($\gamma\text{-WO}_3$, 17–330 °C) → triclinic ($\delta\text{-WO}_3$, -43–17 °C) → monoclinic II ($\varepsilon\text{-WO}_3$, < -43 °C).^{11,12} Among them, the $\gamma\text{-WO}_3$ is the most stable phase in bulk WO_3 at room temperature. Thus, the generally mentioned WO_3 refers in particular to $\gamma\text{-WO}_3$. WO_3 possesses good hole mobility (10 $\text{cm}^2 \text{V}^{-1} \text{s}^{-1}$) and long diffusion length (150 nm), much better than those of $\alpha\text{-Fe}_2\text{O}_3$ (10⁻²–10⁻¹ $\text{cm}^2 \text{V}^{-1} \text{s}^{-1}$ and 2–20 nm).^{13,14} WO_3 has attracted a lot of interest due to its photosensitivity, good electron transport properties, and stability against photocorrosion.¹⁵ However, the conduction band minimum of bulk WO_3 is about 0.4 V (vs NHE at pH = 0) below the hydrogen redox potential,^{16,17} thus, WO_3 photoanode can only drive half of the water splitting reaction for O_2 ; another p-type photocathode (such as p- Cu_2O and p-

Si) or external bias is required for water reduction to obtain H_2 .^{18,19} The photocatalytic reactivity of a semiconductor photocatalyst is affected by its surface environment such as surface electronic and atomic structures, which critically depend on the different crystal facets.²⁰ The surface atomic structure tunable by crystal facet engineering can easily adjust the properties of the semiconductor, such as electronic band structure, surface energy and surface active sites, the adsorption of reactant, and desorption of reaction product.²¹ Guo et al.²² have reported that the preferential orientation of the (002) planes was possibly more favorable in adsorption and redox reaction of pollutants than preferential orientation of the (020) planes. Valdés and Kroes²³ have investigated that photo-oxidation of water on the $\gamma\text{-WO}_3$ surfaces requires 1.04 V overpotential for (200), 1.10 V for (020), and 1.05 V for (002) by using density functional theory (DFT) calculations. Most recently, Xie et al.²⁴ have reported a quasi-cubic-like monoclinic WO_3 crystal with {002}, {200}, and {020} facets, which show a much higher photocatalytic O_2 evolution; a {002}-dominant sheet-like WO_3 can reduce CO_2 to CH_4 under light illumination. Up to now, the active sites at different facets and the underlying reaction mechanisms in photocatalytic

Received: August 16, 2014

Revised: September 29, 2014



processes of WO_3 are still not clear, which attract many researchers' interest.

So far, WO_3 thin films can be made by different methods such as sputtering, evaporation, chemical vapor deposition (CVD), pulsed laser deposition (PLD), electrodeposition, molecular beam epitaxy, sol-gel, hydrothermal reaction, and so on.²⁰ Since the properties of WO_3 crystals sensitively depend on the dominant crystal facets, it is useful to make epitaxial WO_3 films. Much work has been done on investigation of the epitaxial WO_3 films on the different type of substrates such as sapphire,^{25–27} MgO ,²⁵ SrTiO_3 ,²⁷ $\alpha\text{-Al}_2\text{O}_3$,^{25,28,29} substrates by sputtering, CVD, PLD, and electron beam deposition methods. However, these works for making epitaxial WO_3 films are relatively expensive and require extreme experimental conditions such as high temperature and high vacuum. Moreover, these substrates are electrical insulators.²⁰ Recently, Liu et al.^{30,31} have fabricated micropatterned tungsten oxide (WO_2 , WO_3 , and $\text{W}_{18}\text{O}_{49}$) nanowires arrays with the growth direction of $[0\bar{1}1]$ or $[010]$ orientations on conductive Si or indium-doped tin oxide (ITO) substrates with very excellent field emission properties. For using in solar energy conversion devices such as solar cell and solar water splitting system, it is very useful to fabricate the epitaxial WO_3 films on transparent conductive substrates such as ITO and fluorine doped tin oxide (FTO) coated glasses. Compared with ITO coated glass, FTO is better for the substrate because its resistance is more stable than that of ITO in the thermal treatment.³² Perry et al.³³ have synthesized nanoscale $\text{WO}_3\cdot\text{H}_2\text{O}$ platelets by a crash precipitation method. Manukyan et al.³⁴ have reported that $\text{WO}_3\cdot\text{H}_2\text{O}$ nanosheets can be obtained by acid treatment of CaWO_4 sheets, which were produced by controlled self-sustaining reduction of Na_2WO_4 at room temperature. However, the morphologies of the platelets and the nanosheets obtained by these two methods are not uniform. The hydrothermal method is a good method to get uniform WO_3 nano-/microparticles, such as $\text{WO}_3\cdot0.33\text{H}_2\text{O}$ hexagonal-shaped nanodiscs,^{35,36} WO_3 nanorods,³⁶ $\text{WO}_3\cdot0.33\text{H}_2\text{O}$ octahedral-shaped microcrystals,³⁶ and $\text{WO}_3\cdot\text{H}_2\text{O}$ square nanoplates.³⁷ In this work, uniform and high crystalline orthorhombic $\text{WO}_3\cdot\text{H}_2\text{O}$ nanoplates are prepared by the hydrothermal method. The nanoplates can be fabricated on FTO glass and form a (020) facet dominant $\text{WO}_3\cdot\text{H}_2\text{O}$ thin film by a facile rubbing method. After calcination, the (020)-oriented $\text{WO}_3\cdot\text{H}_2\text{O}$ film can be transformed to monoclinic (002)-oriented WO_3 film. Photoelectrochemical properties of (002)-oriented WO_3 films with different thicknesses are carried out comparatively. These works give a method to fabricate WO_3 thin film for the artificial photosynthesis devices by facile rubbing of WO_3 nanoparticles.

2. EXPERIMENTAL SECTION

2.1. Synthesis of $\text{WO}_3\cdot\text{H}_2\text{O}$ Nanoplates. All chemicals were used directly without further purification. $\text{WO}_3\cdot\text{H}_2\text{O}$ nanoplates were synthesized by a simple hydrothermal method. The typical experimental process was carried out as follows: 1.0 g of $\text{Na}_2\text{WO}_4\cdot2\text{H}_2\text{O}$ (SamChun Chemical, $\geq 98\%$) was dissolved in 50 mL of deionized water, and then 0.9 mL of L-lactic acid solution (Aldrich, 50% solution in water) was added as a capping agent and continuously stirred for 10 min to make an homogeneous solution. A white gel type solution was obtained after the pH of the solution was adjusted to 1.0 by adding 6 mol/L HCl aqueous solution. An additional 30 min of stirring was given to make sure that the pH value was invariable. Then the white gel type precursor was transferred into a Teflon-lined stainless steel autoclave (inner volume is about 80 mL). After the autoclave was tightly sealed, it was put into the oven for a reaction at

120 °C for 6, 12, 24, and 36 h. Yellow powder type products were obtained by centrifuge (10000 rpm for 10 min) after three times washing with DI water and ethanol and drying at 60 °C for longer than 6 h. For comparison, the same experiment was carried out at 180 °C for 24 h.

2.2. Fabrication of Dominant WO_3 Thin Films on FTO. The orthorhombic phase (020) ($O(020)$) facet oriented $\text{WO}_3\cdot\text{H}_2\text{O}$ nanoplate film was achieved on FTO surface by rubbing the previously synthesized nanoplate powder on polyethylenimine (PEI, Aldrich, M_w 20000, 99%) ethanol solution coated FTO glass substrate in a similar process as we reported in the previous work.²⁰ PEI ethanol solution (1.0 wt %) was first spin coated (2000 rpm for 20 s, Spin Coater ACE-200) on FTO substrate to produce a sticky ultrathin film. Then, the $\text{WO}_3\cdot\text{H}_2\text{O}$ nanoplate powder was carefully ground into a very thin powder in a mortar and rubbed on PEI layer by finger which was protected by a powder-free latex exam finger cot. The thickness is dependent on the rubbing force and rubbing time. The higher rubbing force and the longer rubbing time used, the thinner film will result. After rubbing, the $O(020)$ -oriented $\text{WO}_3\cdot\text{H}_2\text{O}$ film was obtained regardless of the presence of PEI. The requisite calcination process was done at 500 °C for 2 h in air to remove the organic layer and allow the converted (002) oriented monoclinic phase WO_3 to be tightly connected onto the FTO surface. To know the properties of the films made by rubbing method, three $\gamma\text{-WO}_3$ nanoplate films with the thickness of 120, 190, and 250 nm were selected in this experiment. For comparison, WO_3 particle type thin film was made by spin coating (1500 rpm for 20 s) a solution which was prepared by dissolving 1.5 g of H_2WO_4 and 0.5 g of poly(vinyl alcohol) (PVA) (Aldrich, 99%) in 10 mL of 35 wt % H_2O_2 (Junsei, 35%) on FTO glass, followed by annealing at 500 °C for 2 h in air.

2.3. Characterization. X-ray diffraction (XRD, Rigaku miniFlex-II desktop, Cu K α) patterns, transmission electron microscopy (TEM), and selected area electron diffraction (SAED, JEOL JEM-2100 F) patterns were used to check the crystallinity and crystal structure of the nanoplate powders and films. Thermal gravimetric analysis (TGA) was performed by using a STA N-650 simultaneous thermal analyzer (SCINCO) with a heating rate of 10 °C min $^{-1}$ under Ar (99.999%, SN) flow. Surface and cross-sectional morphologies of samples were obtained using a Hitachi Horiba S-4300 scanning electron microscope (SEM). Raman spectra of the samples were recorded by a homemade setup equipped with an Ar $^+$ ion laser (Spectra-Physics Stabilite 2017) as an excitation beam source, a spectrometer (Horiba Jobin Yvon TRIAX 550), and a CCD detector (Horiba Jobin Yvon Symphony) cooled at –196 °C. The wavelength of the excitation beam was 514.5 nm. X-ray photoelectron spectroscopy (XPS, MultiLab 2000) analyses were performed and calibrated by the binding energy of C 1s 284.6 eV. Diffuse reflectance spectra (DRS) of the samples were recorded on a Varian Cary 5000 UV-vis-NIR spectrophotometer equipped with an integrating sphere using BaSO_4 as a reference. The diffuse reflectance spectra were converted into the absorbance and the Kubelka-Munk (K-M) form. Photoelectrochemical measurements were conducted with a potentiostat/galvanostat (Compactstat, Invium Technologies) in a conventional three-electrode cell in a V-style with quartz window cell at room temperature under 1 sun (Asahi HAL-320 solar simulator) illumination, employing a coiled Pt wire and an Ag/AgCl (in 3 M NaCl) electrode as counter and reference electrode, respectively. A 0.5 M Na_2SO_4 aqueous solution (pH 6.3) was used as electrolyte for all of electrochemical and photoelectrochemical tests. Photocurrent–potential was measured using linear sweep voltammogram (LSV) at a scan rate of 10 mV/s with chopped light (light on and off: 1 Hz). For checking the incident photon to electron conversion efficiency (IPCE) (HS Technologies, Korea), the absolute intensity of the monochromic incident light was measured by a silicon photodiode (model BS-500, Bunkoukeiki Co. Ltd., Japan). Electrochemical impedance spectroscopy (EIS) was checked using a potentiostat/galvanostat (Compactstat, Invium Technologies) in a frequency range of 0.05–10 kHz. The potentials vs Ag/AgCl can be converted to the reversible hydrogen electrode (RHE) scale using the following relationship:^{38,39}

$$E_{\text{RHE}} = E_{\text{Ag}/\text{AgCl}} + E_{\text{Ag}/\text{AgCl vs NHE}}^0 + 0.0591 \times \text{pH} \quad (1)$$

with $E_{\text{Ag}/\text{AgCl vs NHE}}^0 = 0.209 \text{ V}$ at 25°C and $\text{pH} = 6.3$:

$$E_{\text{RHE}} = E_{\text{Ag}/\text{AgCl}} + 0.209 + 0.0591 \times 6.3 \approx E_{\text{Ag}/\text{AgCl}} + 0.58 \text{ V} \quad (2)$$

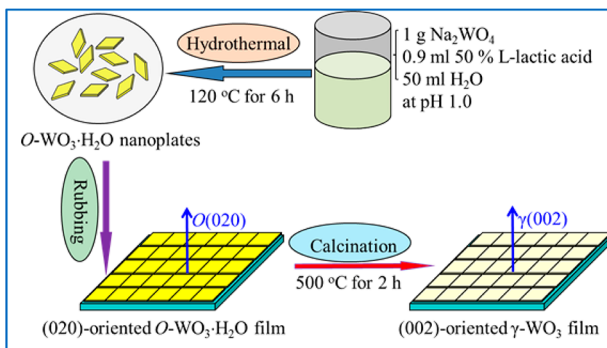
where E_{RHE} is the converted potential vs RHE and $E_{\text{Ag}/\text{AgCl}}$ is the experimental potential measured vs Ag/AgCl reference electrode. For example, the thermodynamic potential for water oxidation ($2\text{H}_2\text{O} \rightarrow \text{O}_2 + 4\text{H}^+ + 4\text{e}^-$, $E_{\text{O}_2/\text{H}_2\text{O}}$ vs NHE = 1.23 V at 25°C) is 0.65 V vs Ag/AgCl at pH = 6.3, which is calculated by eq 2.

3. RESULTS AND DISCUSSION

3.1. Preparation of Nanoplate Particles and Their Characterization.

For controlling the morphology of WO_3 crystals in hydrothermal reaction, some organic acids such as citric acid and oxalic acid were used as capping agents.^{20,40} It was generally considered that the carboxyl functional groups can play an important role for the production of WO_3 particles with specific morphology.⁴¹ In our experiments, the L-lactic acid was used as a capping agent in the hydrothermal reaction process for preparation of rectangular $\text{WO}_3\cdot\text{H}_2\text{O}$ nanoplates. All of the products obtained at 120°C for different reaction times are yellow color. Scheme 1 shows the typical

Scheme 1. Schematic Illustration of the Procedure for Synthesis of $\text{O-WO}_3\cdot\text{H}_2\text{O}$ Nanoplates by Hydrothermal Method, Fabrication of (020)-Oriented $\text{O-WO}_3\cdot\text{H}_2\text{O}$ Nanoplate Thin Film on FTO Glass Substrate by Rubbing Method and Convert the Film to (002)-Oriented $\gamma\text{-WO}_3$ Film by Calcination in Air



experimental procedure for synthesis of $\text{O-WO}_3\cdot\text{H}_2\text{O}$ nanoplates and fabrication of (020)-oriented $\text{O-WO}_3\cdot\text{H}_2\text{O}$ nanoplate thin film on FTO substrates by a facile rubbing method and converting the film to (002)-oriented $\gamma\text{-WO}_3$ by calcination at high temperature in air. Figure 1a–c shows SEM images of $\text{O-WO}_3\cdot\text{H}_2\text{O}$ nanoplate powders obtained at 120°C for different reaction times. The SEM images show that all of the nanoparticles obtained at 6, 12, and 24 h are approximate square nanoplates with a length of ca. 300 nm and thickness of <100 nm. The samples are extremely uniform in large scale as shown in Figure S1, Supporting Information. There are not so many differences in the shape and length of the nanoplates which are obtained at different reaction times; however, the thickness is slightly increased as the reaction time is increased. The average thicknesses, measured in Figure 1a–c, are ca. 41, 49, and 69 nm corresponding to the reaction time of 6, 12, and 24 h, respectively. Figure 1e1–e3 shows XRD patterns of as-prepared $\text{WO}_3\cdot\text{H}_2\text{O}$ powders which can be indexed to the orthorhombic phase (space group: Pmn) $\text{WO}_3\cdot\text{H}_2\text{O}$ with the

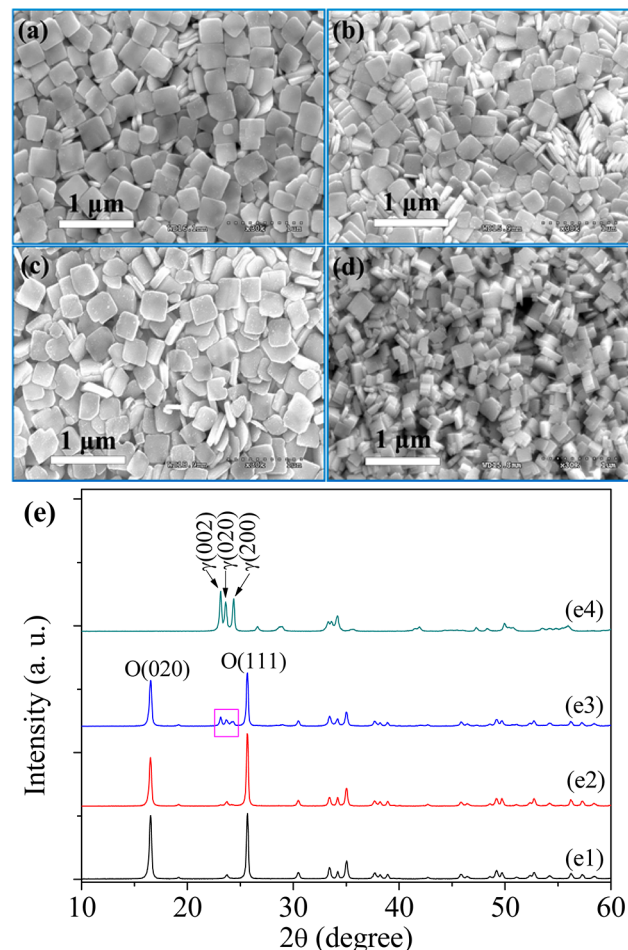


Figure 1. SEM images and XRD patterns of the $\text{WO}_3\cdot\text{H}_2\text{O}$ nanoplate powder samples obtained by the hydrothermal method at different conditions. (a and e1) 120°C for 6 h, (b and e2) 120°C for 12 h, (c and e3) 120°C for 24 h and (d and e4) 180°C for 24 h.

standard card JCPDS no. 43-0679. Two main peaks with high intensities are (020) and (111). It is observed that three characteristic peaks of monoclinic phase WO_3 with very low intensities marked by a magenta rectangle exist in Figure 1e3. It indicates that a little amount of orthorhombic phase $\text{WO}_3\cdot\text{H}_2\text{O}$ can be dehydrated and converted to monoclinic phase WO_3 after a long time (24 h) hydrothermal reaction at 120°C . Yang et al.⁴² have reported that the orthorhombic $\text{WO}_3\cdot\text{H}_2\text{O}$ structure began to transform to the monoclinic WO_3 phase at the hydrothermal temperature of 150°C . To confirm this result, the hydrothermal reaction at 120°C for 36 h was conducted as shown in Figure S2, Supporting Information. It is observed that the intensities of three characteristic peaks of monoclinic phase WO_3 are increased, which indicates that the orthorhombic phase $\text{WO}_3\cdot\text{H}_2\text{O}$ can be transformed to monoclinic phase WO_3 with a long time hydrothermal reaction even at relatively low temperature such as 120°C . The strong and sharp reflection peaks and very horizontal baseline in Figure 1e1,e2 indicates the high crystallinity and purity in the $\text{O-WO}_3\cdot\text{H}_2\text{O}$ powder samples.

The Raman technique is well-suited to the analysis of WO_3 phases (allotropes) as well as the detection of intercalated (structural) and surface adsorbed H_2O for the hydrates ($\text{WO}_3\cdot x\text{H}_2\text{O}$, $x = 1/3, 1, 2$, etc.).^{43,44} The Raman spectra of the as-obtained and annealed $\text{WO}_3\cdot\text{H}_2\text{O}$ nanoplate powder are shown

in Figure 2. The as-obtained $\text{O-WO}_3\cdot\text{H}_2\text{O}$ powder reveals two main Raman peaks at 939.6 and 629.7 cm^{-1} , which correspond

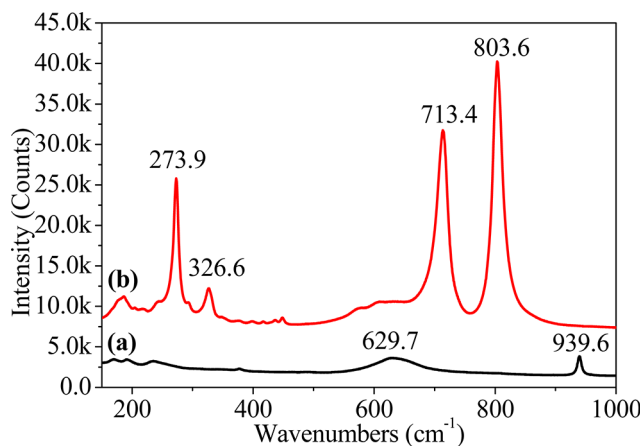


Figure 2. Raman spectra of the $\text{WO}_3\cdot\text{H}_2\text{O}$ nanoplate powder (a) as-obtained at 120 °C for 6 h by hydrothermal reaction and (b) annealed at 500 °C for 2 h in air ($\gamma\text{-WO}_3$).

to stretching modes of terminal W=O and bridging $\text{O}-\text{W}-\text{O}$ bonds, respectively.⁴⁴ After calcination, the Raman spectrum of the annealed WO_3 powder consists of three characteristic regions, less than 200, 200–400, and 600–900 cm^{-1} , which can be indexed to the typical monoclinic WO_3 ($\gamma\text{-WO}_3$) structure.^{45,46} The Raman peaks at 713.4 and 803.6 cm^{-1} are attributable to the $\text{W}-\text{O}-\text{W}$ stretching vibrations in the tungsten oxide network.^{44–46} The $\text{W}-\text{O}-\text{W}$ bending modes of bridging oxide ion peaks appear at 273.9 and 326.6 cm^{-1} .^{44–46} The peaks at 186.5 cm^{-1} correspond to the $(\text{W}_2\text{O}_2)_n$ chains.⁴⁷ The Raman spectra further indicate that the pure $\gamma\text{-WO}_3$ can be formed after calcination of the as-obtained orthorhombic $\text{WO}_3\cdot\text{H}_2\text{O}$.

To identify the component in the as-obtained nanoplates, the EDS spectrum was checked as shown in Figure S3, Supporting Information. The Cl element with a very low atomic ratio can be ignored, and the Na element was not detected. Namely, the nanoplates are only composed of W and O elements. To determine detailed elemental information on samples, the XPS spectra of the $\text{WO}_3\cdot\text{H}_2\text{O}$ and $\gamma\text{-WO}_3$ powders was carried out as shown in Figure 3. The survey scan spectra (Figure 3a) confirm the presence of W, O, and a small amount of C. Carbon could be attributed to the sample preparation (carbon sources in air) and subsequent handling, or the slightly exposed carbon tape which was used for holding samples. No other impurities' signal in both spectra indicates that our method can be used to prepare $\text{WO}_3\cdot\text{H}_2\text{O}$ and $\gamma\text{-WO}_3$ nanoplates with high purity. Four types of W oxidation states, W^{6+} , W^{5+} , W^{4+} , W^{0+} (intermediate state between W^{4+} and W^0) and W^0 , could exist in the tungsten suboxide (WO_x , $0 < x < 3$; such as $\text{W}_{20}\text{O}_{58}$, $\text{W}_{18}\text{O}_{49}$, WO_2 , WO , W_3O , etc.) or the tungsten bronze type compounds (M_xWO_3 , where M = Cs, Rb, K, Na, H, etc.),^{30,31,48–50} which can be investigated by the binding energies of W 4f_{7/2} at the different values: W^{6+} at 35.2–35.7 eV, W^{5+} at 33.9–34.5 eV, W^{4+} at 33.1–33.5, W^{0+} at 31.5 ± 0.1 eV, and W^0 at 30.9 ± 0.1 eV.^{48,49} As shown in the high resolution W 4f core-level spectra (Figure 3b,d), only paired sharp peaks in $\gamma\text{-WO}_3$ were observed at a binding energy of 35.5 and 37.6 eV corresponding to the characteristic W 4f_{7/2} and W 4f_{5/2} peaks for WO_3 , respectively.^{51–53} It also indicates that the

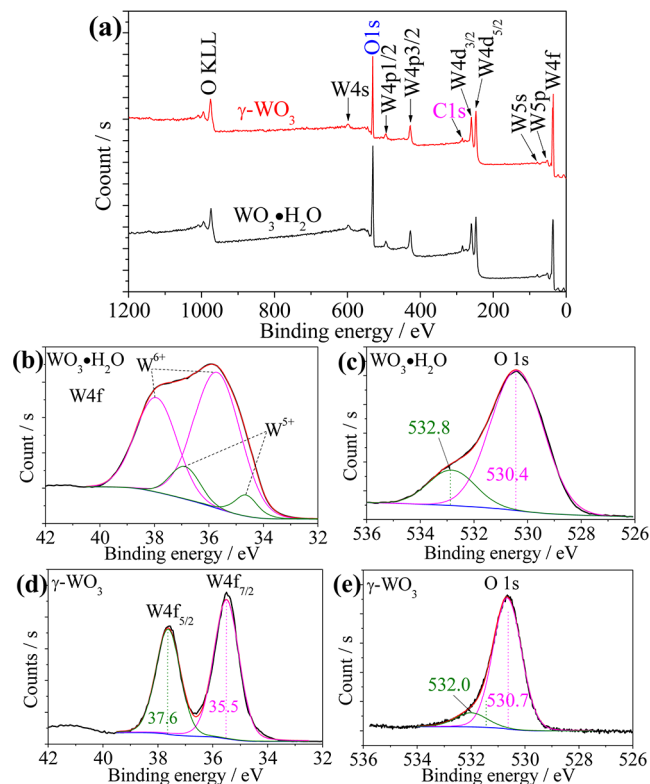


Figure 3. XPS spectra of (a) survey scan, (b, d) W 4f doublet core level and (c, e) O 1s core level high-resolution spectra for $\text{O-WO}_3\cdot\text{H}_2\text{O}$ powder and $\gamma\text{-WO}_3$ powder. The black curves correspond to the experiment data, and they were fitted with the colored curves using an XPS fitting program (XPSPEAK41).

tungsten (W) is fully oxidized and only present in the six-valent oxidation state (W^{6+}).^{51,52} Except one main paired characteristic W 4f_{7/2} and W 4f_{5/2} peak at ca. 35.7 and 37.9 eV for W^{6+} , respectively, other one paired peaks are observed at lower binding energies with values of ca. 34.6 and 36.9 eV, corresponding to the W^{5+} oxidation state.^{48–50} This phenomenon was also observed in nanosheet-assembled $\text{WO}_3\cdot\text{H}_2\text{O}$ microspheres by Bai et al.⁵⁴ The coexistence of W^{6+} and W^{5+} in the surface of $\text{WO}_3\cdot\text{H}_2\text{O}$ indicates that $\text{WO}_3\cdot\text{H}_2\text{O}$ has oxygen deficiency on the surface. It should be noted that $\text{WO}_3\cdot\text{H}_2\text{O}$ easily loses its crystalline H_2O at low temperature (<200 °C). This relatively unstable nature allows the oxygen deficiency to occur. For O 1s core level spectra (Figure 3c,e), each sample contains a main peak at low binding energy and an additional peak at high binding energy, 530.4 and 532.8 eV for $\text{WO}_3\cdot\text{H}_2\text{O}$ and 530.7 and 532.0 eV for $\gamma\text{-WO}_3$, originated from the oxygen bond with W atoms (W–O) in the crystal structure and the -OH bond, respectively. The -OH comes from the surface-adsorbed or interstructure water molecules inside the $\text{WO}_3\cdot\text{H}_2\text{O}$ or the $\gamma\text{-WO}_3$.^{51–53,55} The relative intensity of the additional peak is higher in $\text{WO}_3\cdot\text{H}_2\text{O}$ compared to that in $\gamma\text{-WO}_3$ because of the presence of crystalline water molecules in $\text{WO}_3\cdot\text{H}_2\text{O}$ and the absence of that in $\gamma\text{-WO}_3$ after calcination treatment.

According to our previous works, the pure monoclinic phase WO_3 can be obtained by hydrothermal reaction with a high temperature of 180 °C regardless of the various capping agents.²⁰ To investigate the effect of high temperature, a hydrothermal reaction at 180 °C for 24 h was also carried out. The as-obtained powder is light yellow color. The nanoparticles

are imperfect squares with a large distribution of size from 100 to 300 nm, and they are composed of layered thin plates as shown in Figure 1d. The XRD pattern in Figure 1e4 indicates that the pure monoclinic phase WO_3 ($\gamma\text{-WO}_3$, space group: $Pmn\bar{b}$, JCPDS No. 43-1035) can be obtained at high temperature. To determine the thermal property of $\text{WO}_3\text{-H}_2\text{O}$ in the heat treatment process, thermal gravimetric analysis (TGA) was performed from 30 to 550 °C as shown in Figure 4.

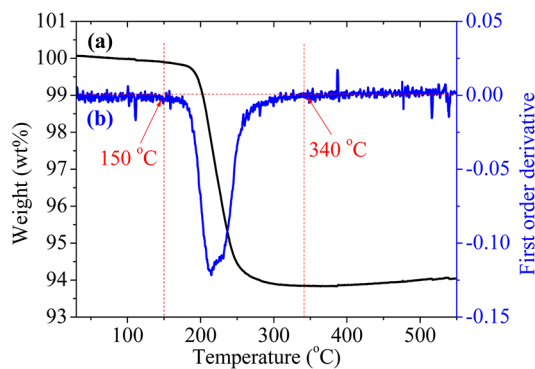


Figure 4. (a) TGA curve and (b) corresponding first-order derivative curve of $\text{WO}_3\text{-H}_2\text{O}$ nanoplate powder.

Two very flat regions in the TGA curve were also observed as the same as M. Gotić et al. reported.⁵⁶ One region between room temperature and 150 °C and another region between 340 and 550 °C of which the first-order derivative is zero are shown, and it indicates the weight loss starts at 150 °C and stops at 340 °C. The total weight loss is 6.18 wt %, which is smaller than 7.20 wt % of the phase composition $\text{WO}_3\text{-H}_2\text{O}$. The possible reason is that a little amount of dehydrated WO_3 exists in the product, or the $\text{WO}_3\text{-H}_2\text{O}$ is dehydrated in the long time drying process. However, the orthorhombic phase $\text{WO}_3\text{-H}_2\text{O}$ can be completely transformed to monoclinic phase WO_3 by calcination at high temperature such as 500 °C for 2 h in air.²⁰ In addition, the WO_3 film annealed at 500 °C in air shows the best photoelectrochemical response due to improved crystallinity and enhanced light absorption in the long-wavelength region. Although the annealed WO_3 film at 600 °C shows better crystallinity and light absorption properties, its amount of electrochemical reaction sites is reduced as Ahn et al. reported.⁵⁷ Therefore, the powder samples and the films were annealed at 500 °C in air for the required characterizations in this work.

More-detailed crystal structural information on the samples with and without heat treatment was carried out by TEM. Figure 5a–i shows the TEM, HR-TEM images, SAED, and fast Fourier transform (FFT) patterns of $\text{WO}_3\text{-H}_2\text{O}$ nanoplate before and after calcination. The TEM image shows that the particle size of the nanoplate is about 250–300 nm. The HR-TEM image and SAED pattern corresponding to the red rectangle area in Figure 5a clearly show that the nanoplate is single crystal with a layered structure. It is easily observed that some layers could be partially broke off. Its crystal lattices of ca. 0.26 nm correspond to the *d*-spacing of (200) facets. After the nanoplate was dehydrated at 500 °C in air, the original phase can be changed to the monoclinic phase WO_3 . Nonuniform contrast in the TEM image indicates some defects on the WO_3 nanoplate surface as shown in Figure 5d, which can be attributed to the inhomogeneous dehydrate process in layered $\text{WO}_3\text{-H}_2\text{O}$ structure. However, the crystallinity was still very

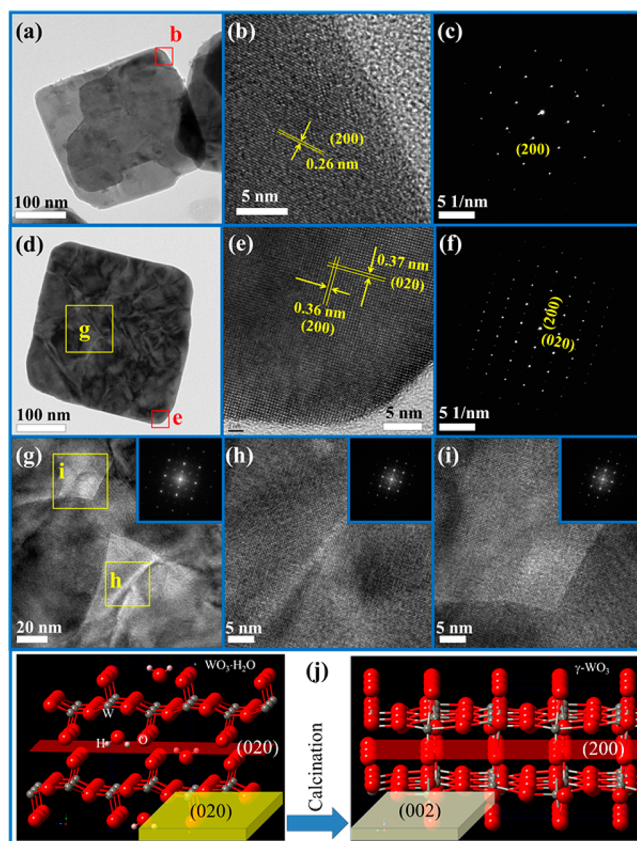


Figure 5. TEM, HR-TEM images, and SAED patterns of (a–c) as-synthesized $\text{WO}_3\text{-H}_2\text{O}$ nanoplate at 120 °C for 6 h, and (d–i) after calcination at 500 °C for 2 h in air. SAED patterns of (c) and (f) correspond to the area in (a) and (d) marked by a red rectangle, respectively. The insets in (g), (h), and (i) are their corresponding FFT images. Panel (j) is a schematic illustration of crystal structure transformation via calcination. Red balls represent O atoms, gray ones are for W atoms.

good. The HR-TEM images, SAED, and FFT patterns as shown in Figure 5e–i and Figure S4a,b indicate that this monoclinic phase WO_3 nanoplate shows a single crystalline property, although some structural defects exist. In Figure 5e, the crystal lattices of 0.36 and 0.37 nm correspond to the *d*-spacing of (200) and (020) facets, respectively. As mentioned above, some layers in the initial $\text{WO}_3\text{-H}_2\text{O}$ nanoplates are not perfect. In addition, some parts of the nanoplates also can be broken by calcination process. The defects in the $\gamma\text{-WO}_3$ are mainly attributed to these two reasons. It is noted that some cracked parts attach onto the $\gamma\text{-WO}_3$, which makes some parts of the nanoplates also show polycrystalline properties as shown in Figure S4c–f, Supporting Information. From the HR-TEM images and SAED patterns, it is concluded that the largest exposed (020) facet of orthorhombic $\text{WO}_3\text{-H}_2\text{O}$ nanoplate can be converted to the (002) facet of monoclinic WO_3 after dehydration via calcination as the schematic illustration of crystal structure transformation shown in Figure 5j. The similar evolution of preferred orientation from [010] (monoclinic $\text{H}_2\text{WO}_4\text{-H}_2\text{O}$ and orthorhombic $\text{WO}_3\text{-H}_2\text{O}$) to [001] (monoclinic WO_3) have been reported by Chen et al.⁵⁸ and Zhang et al.⁵⁹

One of the most important characteristics of a semiconductor material is its band gap energy (E_g). For determining the E_g , the optical tool applied to measure calculates the

intercept of the extrapolated linear fit in the experiment data of the Tauc plot, $(F(R)h\nu)^m$ versus incident photon energy ($h\nu$) near the absorption edge,⁶⁰ in which $F(R)$ is the absorption coefficient of the material that was converted from the diffuse reflectance (light scattered to all angles) by the Kubelka–Munk function, $F(R) = (1-R)^2/(2R)$, where R is reflectance,⁶¹ m is the inverse of a value of n in the normal Tauc relation,

$$(F(R))h\nu = A_0(h\nu - E_g)^n$$

where

$$A_0 = \left[\frac{e^2}{nch^2 m_e} \right] (2m_r)^{3/2}$$

where A_0 is constant, m_e^* and m_r are the effective and reduced masses of charge carriers, respectively, c is the speed of light in a vacuum, h is the Planck's constant, and n depends on the nature of band transition.^{62,63} The value of the exponent m ($m = 1/n$) is also determined from the nature of the optical transition. $m = 1/2$ or $1/3$ for indirect allowed and indirect forbidden transitions, respectively; $m = 2$ or $2/3$ for direct allowed and direct forbidden transitions, respectively. Figure 6 shows UV–

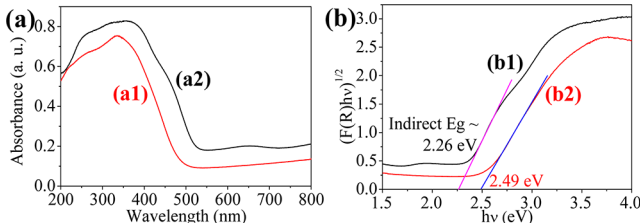


Figure 6. (a) The DRS spectra and (b) the Tauc plots, $((F(R)h\nu)^m$ versus $h\nu$, $m = 1/2$ for the indirect band gap of the $\text{WO}_3\text{-H}_2\text{O}$ nanoplate powder obtained at 120°C for 6 h before (dark curves: a1 and b1) and after (red curves: a2 and b2) calcination at 500°C for 2 h in air.

visible light absorption spectra and Tauc plots of $\text{WO}_3\text{-H}_2\text{O}$ nanoplate powder before and after calcination. The spectra were calculated from the diffuse reflectance data. The absorption onsets of $\text{O-WO}_3\text{-H}_2\text{O}$ and $\gamma\text{-WO}_3$ occurred near 520 and 480 nm, respectively. It indicates that the E_g of $\gamma\text{-WO}_3$ nanoplate is higher than that of $\text{O-WO}_3\text{-H}_2\text{O}$ nanoplate. One observed evidence was that the color of the $\text{O-WO}_3\text{-H}_2\text{O}$ powder changed from yellow to light yellow after the calcination. The experimental E_g values of WO_3 are in the range from ca. 2.6 to 3.2 eV due to variations of the WO_3 structure and the model which has been used to extract E_g . In particular, values of $E_g < 3$ eV are mostly obtained assuming an indirect band gap.^{64,65} In addition, it is known that crystalline, monoclinic WO_3 films have energy band gaps varying from 2.4 to 2.7 eV.⁶⁶ Herein, the indirect band gap energies were extracted for $\text{O-WO}_3\text{-H}_2\text{O}$ and $\gamma\text{-WO}_3$ nanoplate powders by plotting $(F(R)h\nu)^{1/2}$ vs $h\nu$ as shown in Figure 6. The indirect allowed band gap energies for the $\text{O-WO}_3\text{-H}_2\text{O}$ nanoplate and the $\gamma\text{-WO}_3$ nanoplate are ca. 2.26 and 2.49 eV, respectively.

As in previous reports, the (002) facet of monoclinic WO_3 is the most unstable facet with the highest surface energy compared to the other low index crystal facets such as (020) and (200).²⁴ The surface energy (γ) of a crystalline solid can be obtained from the following equation:

$$\gamma = \left(E_{\text{slab}} - \frac{N}{n} E_{\text{bulk}} \right) / 2A$$

where E_{slab} is the total energy of material which contains a surface in particular direction, E_{bulk} stands for total energy of bulk structure, N is the total number of atoms in a unit cell, n denotes the total number of atom in the bulk unit cell, and A is the area of surface of material. For calculation of the three mainly exposed low index crystal facets in monoclinic WO_3 nanoplate, (002), (020), and (200), the unit cell is chosen to contain 64 atoms, while the bulk WO_3 has 32 atoms in the monoclinic unit cell. Each system has an oxygen terminated surface, and the stoichiometric ratio is conserved. Figure 7a–d

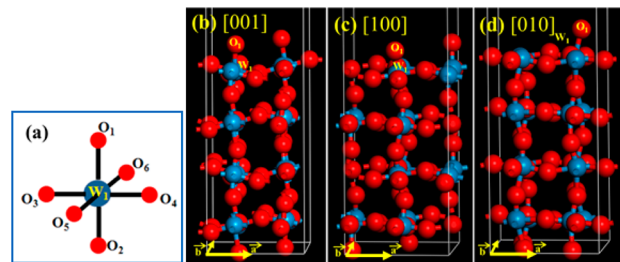


Figure 7. (a) Schematic illustrations of unit cell structures of bulk unit cell, and three different surface geometries such as (b) WO_3 (001), (c) WO_3 (100), (d) WO_3 (010) systems. Note that red balls represent O atoms and blue ones are for W atoms.

shows the schematic illustrations of unit cell structures of bulk unit cell and three different surface geometries such as WO_3 (001), WO_3 (100), WO_3 (010) systems, respectively. The detailed calculation process is introduced in the Supporting Information. The surface energy order is {001} (1.7367 J/m^2) > {010} (1.1152 J/m^2) > {100} (0.6516 J/m^2), which indicates that the largest surface energy is (001) facet in WO_3 as the most reactive facet. The similar result was reported on a surface energy order of {002} (1.56 J m^{-2}) > {020} (1.54 J m^{-2}) > {200} (1.43 J m^{-2}) by Xie et al.²⁴ Indeed, the surface reconstruction is observed after structure optimization, and this surface rearrangement induces modification of electronic structure of material. Because of this feature, the most reactive surface is {002} plane in the $\gamma\text{-WO}_3$ crystal.

3.2. Fabrication of WO_3 Nanoplates Thin Films by the Rubbing Method and Their Photoelectrochemical Properties. Now, the rubbing method becomes a significant way to fabricate rapidly and economically the nano-/submicro-/microparticles with mono-/multilayer or one-orientation on solid substrates, such as glass, Si wafer, TCO glasses, and even some other substrates with smooth surface, without using solvents, reactors, or equipment.^{20,67–69} Herein, we fabricated the $\text{O-WO}_3\text{-H}_2\text{O}$ nanoplates on FTO glass substrate to form the $\gamma\text{-WO}_3$ thin films with different thicknesses by finger rubbing and postcalcination. Figure 8 shows the top-view and cross-sectional SEM images of three $\gamma\text{-WO}_3$ nanoplate films, named R1, R2, and R3 with thicknesses of 120, 190, and 250 nm, respectively. For easy acquiring of the thickness information on these three samples, we can name them as R1-120, R2-190, and R3-250, respectively. It is observed that the nanoplates on the rubbing sample also cover the entire surface as well, and almost all the nanoplate particles expose their largest facet of (002). Some nanoplates were easily broken by a rubbing force such as pressure and tension; there are two possible reasons to explain that (i) the thicknesses of

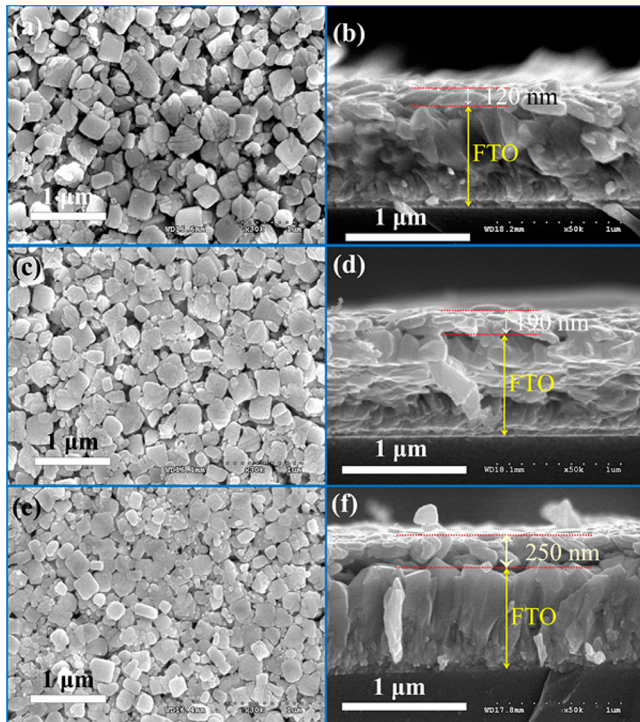


Figure 8. (a, c, e) Top-view and (b, d, f) cross-sectional SEM images of the (002)-oriented γ -WO₃ films with different thicknesses on FTO substrates prepared by rubbing combined with the calcination method using the WO₃·H₂O nanoplates powder. (a, b) The film with the thickness of 120 nm (R1-120), (c, d) the film with the thickness of 190 nm (R2-190) and (e, f) the film with the thickness of 250 nm (R3-250).

nanoplates are ca. 40 nm as shown in Figure 1a, and they can only support the limited force; (ii) the surface of FTO substrate is very rough at the nanoscale level. There are many polyhedral tips as the SEM image shows in Figure S5, Supporting Information; they give an enhanced destruction effect.

The corresponding XRD patterns of rubbing films before and after calcination are shown in Figure 9. The peaks of XRD patterns (Figure 9a–c) of the rubbing O-WO₃·H₂O films, except the ones corresponding to the FTO substrate marked by the stars, show only two main peaks of (020) and (040) indexed by the same JCPDS No. 43-0679. It indicates that the (020)-oriented O-WO₃·H₂O nanoplate film can be prepared by the facile rubbing method. After calcination at high temperature, the peaks of XRD patterns (Figure 9d–f) of the postcalcinated films only show two main peaks of γ -(002) and γ -(004), which can be indexed by the monoclinic phase JCPDS No. 43-1035. Therefore, the (020)-oriented orthorhombic O-WO₃·H₂O nanoplate films can be easily converted to (002)-oriented monoclinic WO₃ films.

Figure S6a, Supporting Information shows the transmittance spectra of the (002)-oriented γ -WO₃ films with the thicknesses of 120, 190, and 250 nm. Compared the bare FTO substrate, all the transmittance intensities of the R1-120, R2-190, and R3-250 were decreased within the visible light region. In addition, the transmittance intensities of γ -WO₃ films slowly decrease with the increase of the thickness of WO₃ layers. However, all the transmittance intensities of the films were kept at ca. 60% in the wavelength range from 470 to 800 nm. Figure 9g is a corresponding digital photograph of (002)-oriented γ -WO₃ films. Figure S6b shows UV-vis absorption spectra of the γ -

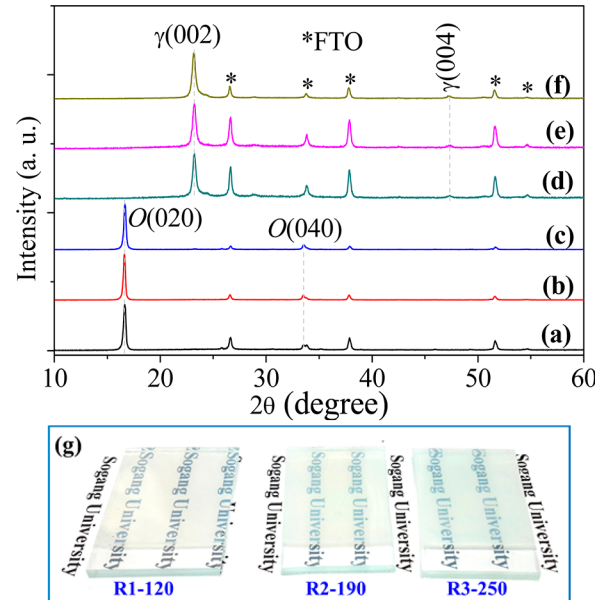


Figure 9. XRD patterns of (a–c) the as-obtained O-WO₃·H₂O films by rubbing and (d–f) the corresponding γ -WO₃ films, R1, R2, and R3, obtained by calcination treatment, respectively. (g) The digital photograph of the samples.

WO₃ films calculated from the DRS data. For S1, S2, and S3, all the absorption onsets occurred near 480 nm. Band gap energies of these films are similar to the value of ca. 2.58 eV referring to an indirect band gap of purely crystalline WO₃. These values were determined using Tauc plots as the same way as the aforementioned explanation. The band gap energies of γ -WO₃ nanoplate films are slightly larger compared to the powder type. It can be attributed to the quantum confinement effect. It is easily observed that the surface of nanoplates became rough and form many defects after calcination as shown in Figure 8a,c,e.

For revealing the superiority of the thin epitaxial (002)-oriented WO₃ film prepared by the rubbing method in photoelectrochemical application for water splitting, a (200) dominant γ -WO₃ film was prepared by the spin coating method as the similar process of the reported work as shown in Figure 10.⁴⁰ The homogeneous WO₃ film is composed of particles with a size of <150 nm and has the same thickness of 120 nm as that of R1-120, named SC-120. It is observed that the spin-coated film has the dominant crystal facet with (200) as shown in Figure 10c2. As the thickness of film is increased to ~700 nm by several spin-annealing cycles, the (200)-oriented epitaxial performance can be relatively enhanced, while the other facets are also exposed clearly as the XRD pattern shown in ref 40. Figure 11 shows the photocurrents and photoresponses of γ -WO₃ films prepared by spin coating and rubbing method under 1 sun illumination (Asahi HAL-320 Sun simulator). As the potential scans to the positive direction from -0.2 to 1.5 V vs Ag/AgCl, anodic photocurrents are observed. It is a typical photocurrent behavior of n-type semiconductor. The photocurrent of γ -WO₃ rubbing electrode is enhanced as the film thickness is increased, following the order of R1-120 < R2-190 < R3-250. Herein, the thickness of 250 nm is less than the optimized thickness of γ -WO₃, which has the shortest charge carrier transport length thus reducing the rate of effective recombination of electron–hole pairs.¹⁷ The photocurrent depending on the thickness of film is similar as the reported

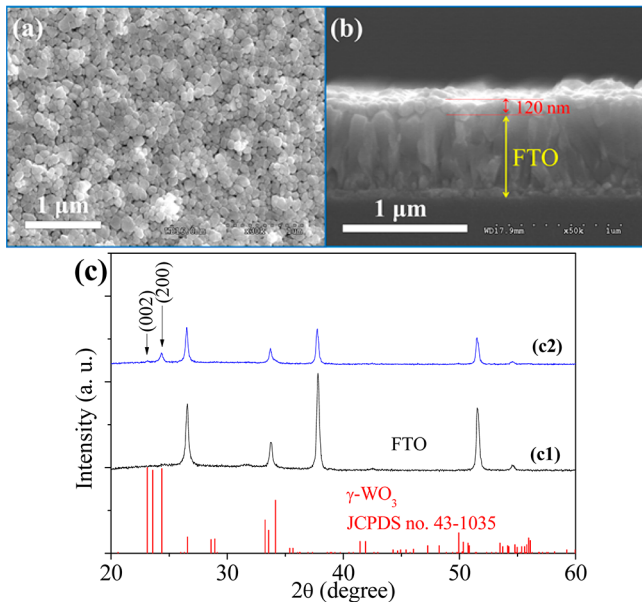


Figure 10. (a) Top-view and (b) cross-sectional SEM images and (c) XRD pattern of the WO₃ thin film prepared by the spin-coating method. (c1) XRD pattern of bare FTO glass.

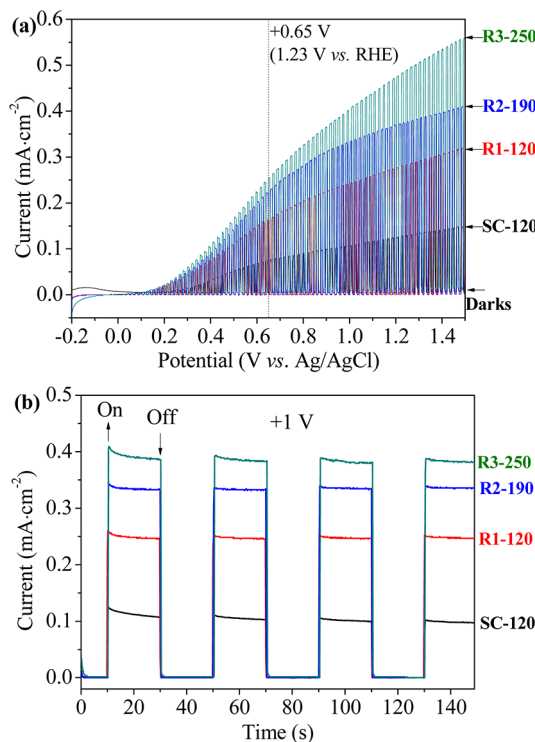


Figure 11. (a) Photocurrents and (b) photoresponse at +1 V vs Ag/AgCl of the different films under 1 sun illumination.

works.⁷⁰ Photocurrents of R1, R2, and R3 are 164, 224, and 250 μA/cm² at 0.65 V vs Ag/AgCl (1.23 V vs RHE), respectively. All photocurrents of three samples are slightly decreased after 120 s intermittent light illumination, which indicates that the films are not rigorously stable as shown in Figure 11b. The reason is that the WO₃ does not possess good chemical stability at pH > 4 under solar illumination.⁵ The photocurrents after 150 s photoresponse are 0.25, 0.34, and 0.38 mA/cm² at +1.0 V vs Ag/AgCl, corresponding to R1-120, R2-190, and R3-250,

respectively. Although the photocurrents are rather low compared to many other literature results, they are comparable to the values of some films such as the WO₃ nanowire film (ca. 0.2 mA/cm² at 1.0 V) reported by Grimes's group,⁷¹ the pristine nanoflake WO₃ film (0.1 mA/cm² at +1.0 V), and the hydrogen-treated nanoflake WO₃ films (ca. 0.22 and 0.45 mA/cm² at +1.0 V) reported by Li's group.⁵² For comparison, the photoelectrochemical properties of spin-coated WO₃ film with the thickness of 120 nm (SC-120) is also carried out. The photocurrent of spin-coated WO₃ film, ca. 73 μA/cm² at +0.65 V, is lower than that half of R1-120 even with the same thickness.

To know the reason for the different photoelectrochemical performance, the incident photon to electron conversion efficiency (IPCE) determination was carried out at +0.65 V vs Ag/AgCl under monochromic light illumination as shown in Figure 12a.

$$\text{IPCE} = \frac{1240 \times j_p (\text{mA}/\text{cm}^2)}{P(\text{mW}/\text{cm}^2) \times \lambda (\text{nm})} \times 100\%$$

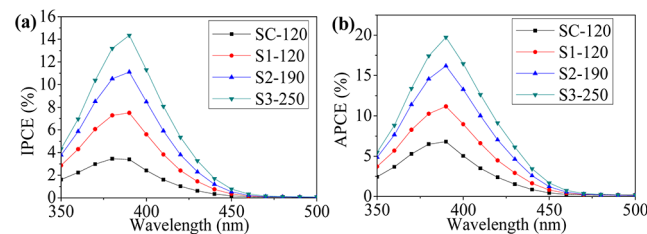


Figure 12. (a) IPCE for (a) spin-coating WO₃/FTO film (SC-120), (b) WO₃ films prepared by rubbing method: S1-120, S2-190, and S3-250. IPCEs were conducted in 0.5 M Na₂SO₄ solution at +1.0 V vs Ag/AgCl.

where J_p is the photocurrent density, P is the incident photon flux density at the photoelectrode location, and λ is wavelength. IPCE does not take into account the light harvesting efficiency of photoelectrode; it is not well suitable for detailed discussion of the photocurrent conversion process. IPCE can be converted to absorbed photon to current conversion efficiency (APCE) as shown in Figure 12b. APCEs are evaluated from IPCEs and light harvesting efficiency based on the following equation:⁷²

$$\text{APCE} = \frac{\text{IPCE}}{1 - T} = \frac{\text{IPCE}}{1 - 10^{-A}}$$

where T is the transmittance and A is the absorbance of the exciting light. All the onsets of IPCE are similar, about 480 nm, which is in agreement with the previous report.⁵³ The order of IPCE values of four samples is matched with the order of photocurrent values, SC-120 < R1-120 < R2-190 < R3-250, with the maximum IPCE values of 3.5%, 7.5%, 11.1%, and 14.3% at 390 nm, respectively. The corresponding APCE values are 6.8, 11.2, 16.2, and 19.7%, respectively. It is interesting that the WO₃ films with a similar thickness of 120 nm give very different electrochemical performances. Especially, to determine the difference between those two kinds of electrodes (SC-120 and R1-120), their interfacial charge-transfer resistances (R_{ct}) are checked at 1.0 V vs Ag/AgCl with or without 1 sun light illumination as shown in Figure 13.

With similar phenomena in the previous report, the R_{ct} of two samples without light illumination tends to infinity.⁵³ It indicates that very few charges can pass through the interface

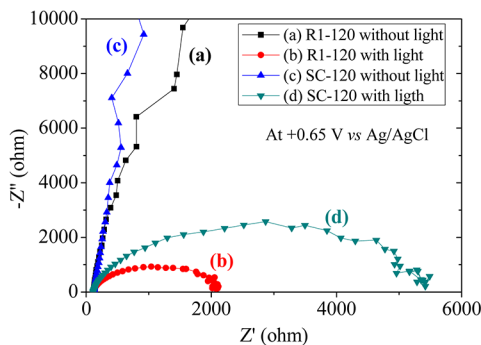


Figure 13. Electrochemical impedance spectra (EIS) of WO_3 thin films on FTO substrates prepared by (a, b) rubbing (R1-120) and (c, d) spin-coating (SC-120) with and without 1 sun light illumination. EIS was conducted in 0.5 M Na_2SO_4 solution at +0.65 V vs Ag/AgCl.

between the electrode and the electrolyte under dark even at the applied potential of +0.65 V vs Ag/AgCl. In other words, the dark currents of these two films are almost zero in a big potential scanning range as shown in Figure 10a, which can be attributed to infinite R_{ct} . With light illumination, photo-generated charge carriers (electrons and holes) are separated by applied potential. The R_{ct} can be reduced; meanwhile electronic conductivities of WO_3 electrodes were enhanced under light illumination.⁵³ The diameter of arc radius on the EIS Nyquist plot of the R1-120 is smaller than that of SC-120. It indicates that the conductivity of R1-120 is much larger than that of SC-120. The two possible reasons are explained as follows: (1) The SC-120 film is more compact than the R1-120 film as shown in Figures 8a and 10a. Gaps existing between nanoplates can give large interfacial heterojunction (WO_3 /electrolyte) area, which can enhance the conductivity. The larger conductivity of the film, the more photocurrent can be produced.⁵³ (2) The R1 is (002)-oriented film, while the SC-120 is (200) dominant film. As mentioned above, the (002) plane is the most reactive surface among three low index crystal facets of (002), (020), and (200) in $\gamma\text{-WO}_3$ crystal; therefore, the charge carries can be easily transferred between the electrolyte/ WO_3 , WO_3 /FTO interfaces. In a word, the (002) facet dominant WO_3 thin films prepared by facile rubbing gives a better photoelectrochemical performance compared with the WO_3 thin film prepared by spin-coating with same thickness.

4. CONCLUSIONS

In this work, highly crystalline pure orthorhombic $\text{WO}_3\text{-H}_2\text{O}$ nanoplates with a clear shape and uniform size distribution have been synthesized by the hydrothermal method using L-lactic acid as the capping agent. The orthorhombic phase $\text{WO}_3\text{-H}_2\text{O}$ can be converted to monoclinic phase WO_3 by calcination at high temperature; in particular, the most exposed (020) facet of the $O\text{-}\text{WO}_3\text{-H}_2\text{O}$ nanoplate is transformed to the most reactive (002) facet of $\gamma\text{-WO}_3$ nanoplate. Band gap energies of the $O\text{-}\text{WO}_3\text{-H}_2\text{O}$ and $\gamma\text{-WO}_3$ nanoplates are ca. 2.26 and 2.49 eV, respectively. The surface energy order of $\gamma\text{-WO}_3$ nanoplate is $\{001\}$ (1.7367 J/m²) > $\{010\}$ (1.1152 J/m²) > $\{100\}$ (0.6516 J/m²). The (002) facet in WO_3 has the largest surface energy. The rubbing method combined with postcalcination has been used to fabricate nanoplates on FTO substrates to form (002)-oriented dominant films. The photocurrent of the (002)-oriented WO_3 film with a thickness of 250 nm can reach 0.38 mA/cm² at +1.0 V vs Ag/AgCl. In the case of the same thickness, the rubbed dominant thin film is much better than

the thin film prepared by spin coating. This work can be a good example to facilely fabricate and study the WO_3 films with (002)-dominant crystal facets for artificial photosynthesis.

■ ASSOCIATED CONTENT

S Supporting Information

The details of surface energy calculation and additional characterization (Figures S1–S6): Low magnification SEM images and EDS spectrum of $\text{WO}_3\text{-H}_2\text{O}$ samples, XRD pattern, and SEM image of $\text{WO}_3\text{-H}_2\text{O}$ sample obtained at 120 °C for 36 h, HR-TEM and FFT images of a polycrystalline $\gamma\text{-WO}_3$ nanoplate, SEM images of the bare FTO glass and transmittance and absorbance spectra of $\gamma\text{-WO}_3$ films. This material is available free of charge via the Internet at <http://pubs.acs.org>.

■ AUTHOR INFORMATION

Corresponding Author

*E-mail: yskang@sogang.ac.kr.

Notes

The authors declare no competing financial interest.

■ ACKNOWLEDGMENTS

This work financially supported by the Korea Center for Artificial Photosynthesis (KCAP) located in Sogang University (No. 2009-0093885) and the Center for Next Generation Dye-sensitized Solar Cells (No. 2008-0061903) funded by the Minister of Science, ICT and Future Planning (MSIP) through the National Research Foundation of Korea and the Brain Korea 21 Plus Project 2014.

■ REFERENCES

- Jiao, Z.; Wang, X.; Wang, J.; Ke, L.; Demir, H. V.; Koh, T. W.; Sun, X. W. *Chem. Commun.* **2012**, 48, 365–367.
- Feng, W.; Wu, G.; Gao, G. *J. Mater. Chem. A* **2014**, 2, 585–590.
- Kida, T.; Nishiyama, A.; Hua, Z.; Suematsu, K.; Yuasa, M.; Shimano, K. *Langmuir* **2014**, 30, 2571–2579.
- Zhang, X.; Lu, X.; Shen, Y.; Han, J.; Yuan, L.; Gong, L.; Xu, Z.; Bai, X.; Wei, M.; Tong, Y.; Gao, Y.; Chen, J.; Zhou, J.; Wang, Z. L. *Chem. Commun.* **2011**, 47, 5804–5806.
- Liu, X.; Wang, F.; Wang, Q. *Phys. Chem. Chem. Phys.* **2012**, 14, 7894–7911.
- Fujishima, A.; Honda, K. *Nature* **1972**, 238, 37–38.
- Wolcott, A.; Smith, W. A.; Kuykendall, T. R.; Zhao, Y.; Zhang, J. Z. *Adv. Funct. Mater.* **2009**, 19, 1849–1856.
- Sivula, K.; Formal, F. L.; Grätzel, M. *ChemSusChem* **2011**, 4, 432–449.
- Park, Y.; McDonald, K. J.; Choi, K. S. *Chem. Soc. Rev.* **2013**, 42, 2321–2337.
- Bignozzi, C. A.; Caramori, S.; Cristina, V.; Argazzi, R.; Meda, L.; Taccia, A. *Chem. Soc. Rev.* **2013**, 42, 2228–2246.
- Salje, E. *Acta Crystallogr.* **1977**, B33, 574–577.
- Zheng, H. D.; Ou, J. Z.; Strano, M. S.; Kaner, R. B.; Mitchell, A.; Kalantar-zadeh, K. *Adv. Funct. Mater.* **2011**, 21, 2175–2196.
- Kennedy, J. H.; Frese, K. W., Jr. *J. Electrochem. Soc.* **1978**, 125, 709–714.
- Butler, M. A. *J. Appl. Phys.* **1977**, 48, 1914–1920.
- Wang, F.; Valentin, C. D.; Pacchioni, G. *J. Phys. Chem. C* **2012**, 116, 8901–8909.
- Bamwenda, G. R.; Arakawa, H. *Appl. Catal., A* **2001**, 210, 181–191.
- Zheng, J. Y.; Song, G.; Kim, C. W.; Kang, Y. S. *Electrochim. Acta* **2012**, 69, 340–344.
- Chen, Q. P.; Li, J. H.; Li, X. J.; Huang, K.; Zhou, B. X.; Cai, W. M.; Shangguan, W. F. *Environ. Sci. Technol.* **2012**, 46, 11451–11458.

- (19) Coridan, R. H.; Shaner, M.; Wiggenhorn, C.; Brunschwig, B. S.; Lewis, N. S. *J. Phys. Chem. C* **2013**, *117*, 6949–6957.
- (20) Zheng, J. Y.; Song, G.; Kim, C. W.; Kang, Y. S. *Nanoscale* **2013**, *5*, 5279–5282.
- (21) Tu, W.; Zhou, Y.; Zou, Z. *Adv. Mater.* **2014**, *26*, 4607–4626.
- (22) Guo, Y.; Quan, X.; Lu, N.; Zhao, H.; Chen, A. S. *Environ. Sci. Technol.* **2007**, *41*, 4422–4427.
- (23) Valdés, Á.; Kroes, G. J. *J. Chem. Phys.* **2009**, *130*, 114701.
- (24) Xie, Y. P.; Liu, G.; Yin, L.; Chen, H. M. *J. Mater. Chem.* **2012**, *22*, 6746–6751.
- (25) Kobayashi, Y.; Terada, S.; Kubota, K. *Thin Solid Films* **1989**, *168*, 133–139.
- (26) Tagtstrom, P.; Jansson, U. *Thin Solid Films* **1999**, *352*, 107–113.
- (27) Garg, A.; Leake, J. A.; Barber, Z. H. *J. Phys. D: Appl. Phys.* **2000**, *33*, 1048–1053.
- (28) Yamamoto, S.; Inouye, A.; Yoshikawa, M. *Nucl. Instrum. Methods Phys. Res., Sect. B* **2008**, *266*, 802–806.
- (29) Mohammad, A. A. *Vacuum* **2009**, *83*, 1326–1332.
- (30) Liu, F.; Li, L.; Mo, F.; Chen, J.; Deng, S.; Xu, N. *Cryst. Growth Des.* **2010**, *10*, 5193–5199.
- (31) Liu, F.; Mo, F. Y.; Jin, S. Y.; Li, L.; Chen, Z. S.; Sun, R.; Chen, J.; Deng, S. Z.; Xu, N. S. *Nanoscale* **2011**, *3*, 1850–1854.
- (32) Kawashima, T.; Matsui, H.; Tanabe, N. *Thin Solid Films* **2003**, *445*, 241–244.
- (33) Perry, W. L.; Smith, B. L.; Bulian, C. J.; Busse, J. R.; Macomber, C. S.; Dye, R. C.; Son, S. F. *Propellants, Explos., Pyrotech.* **2004**, *29*, 99–105.
- (34) Manukyan, K. V.; Voskanyan, A. A.; Rouvimov, S.; Mukasyan, A. S.; Kharatyan, S. L. *J. Mater. Res.* **2013**, *28*, 2611–2621.
- (35) Zhou, L.; Zou, J.; Yu, M.; Wei, J.; Qian, Y.; Wang, Y. *Cryst. Growth Des.* **2008**, *8*, 3993–3998.
- (36) Shi, J.; Hu, G.; Cong, R.; Bu, H.; Dai, N. *New J. Chem.* **2013**, *37*, 1538–1544.
- (37) Miao, B.; Zeng, W.; Xu, S.; Zeng, S.; Chen, Y.; Wu, S. *Mater. Lett.* **2013**, *113*, 13–16.
- (38) Tong, L.; Iwase, A.; Nattestad, A.; Bach, U.; Weidelener, M.; Götz, G.; Mishra, A.; Bäuerle, P.; Amal, R.; Wallace, G. G.; Mozer, A. J. *Energy Environ. Sci.* **2012**, *5*, 9472–9475.
- (39) Read, G.; Park, Y.; Choi, K. S. *J. Phys. Chem. Lett.* **2012**, *3*, 1872–1876.
- (40) Su, J.; Guo, L.; Bao, N.; Grimes, C. A. *Nano Lett.* **2011**, *11*, 1928–1933.
- (41) Wang, N.; Wang, D.; Li, M.; Shi, J.; Li, C. *Nanoscale* **2014**, *6*, 2061–2066.
- (42) Yang, J.; Li, W.; Li, J.; Sun, D.; Chen, Q. *J. Mater. Chem.* **2012**, *22*, 17744–17752.
- (43) Sadek, A. Z.; Zheng, H.; Breedon, M.; Bansal, V.; Bhargava, S. K.; Latham, K.; Zhu, J.; Yu, L.; Hu, Z.; Spizzirri, P. G.; Włodarski, W.; Kalantar-Zadeh, K. *Langmuir* **2009**, *25*, 9545–9551.
- (44) Daniel, M. F.; Desbat, B.; Lassegues, J. C.; Gerand, B.; Figlarz, M. *J. Solid State Chem.* **1987**, *67*, 235–247.
- (45) Clara, S.; Marek, O.; Martine, U.; Jan, A. *J. Am. Chem. Soc.* **2001**, *123*, 10639–10649.
- (46) Yang, Z.; Ni, X. *Langmuir* **2012**, *28*, 4829–4834.
- (47) Pecquenard, B.; Lecacheaux, H.; Livage, L.; Julien, C. *J. Solid State Chem.* **1998**, *135*, 159–168.
- (48) Bigey, C.; Hilaire, L.; Maire, G. *J. Catal.* **1999**, *184*, 406–420.
- (49) Yue, C.; Zhu, X.; Rigutto, M.; Hensen, E. *Appl. Catal. B: Environ.* **2015**, *163*, 370–381.
- (50) Guo, C.; Yin, S.; Yan, M.; Kobayashi, M.; Kakihana, M.; Sato, T. *Inorg. Chem.* **2012**, *51*, 4763–4771.
- (51) Sivakumar, R.; Gopalakrishnan, R.; Jayachandran, M.; Sanjeeviraja, C. *Smart Mater. Struct.* **2006**, *15*, 877–888.
- (52) Wang, G.; Ling, Y.; Wang, H.; Yang, X.; Wang, C.; Zhang, J. Z.; Li, Y. *Energy Environ. Sci.* **2012**, *5*, 6180–6187.
- (53) Li, W.; Li, J.; Wang, X.; Luo, S.; Xiao, J.; Chen, Q. *Electrochim. Acta* **2010**, *56*, 620–625.
- (54) Bai, S.; Zhang, K.; Wang, L.; Sun, J.; Luo, R.; Li, D.; Chen, A. J. *Mater. Chem. A* **2014**, *2*, 7927–7934.
- (55) Zheng, J. Y.; Van, T. K.; Pawar, A. U.; Kim, C. W.; Kang, Y. S. *RSC Adv.* **2014**, *4*, 18616–18620.
- (56) Gotić, M.; Ivanda, M.; Popović, S.; Musić, S. *Mater. Sci. Eng. B* **2000**, *B77*, 193–201.
- (57) Ahn, K. S.; Lee, S. H.; Dillon, A. C.; Tracy, C. E.; Pitts, R. J. *Appl. Phys.* **2007**, *101*, 093524.
- (58) Chen, D.; Gao, L.; Yasumori, A.; Kuroda, K.; Sugahara, Y. *Small* **2008**, *10*, 1813–1822.
- (59) Zhang, H.; Duan, G.; Li, Y.; Xu, X.; Dai, Z.; Cai, W. *Cryst. Growth Des.* **2012**, *12*, 2646–2652.
- (60) Misho, R. H.; Murad, W. A. *Sol. Energy Mater. Sol. Cells* **1992**, *27*, 335–345.
- (61) Kubelka, P.; Munk, F. *Technol. Phys. (Leipzig)* **1931**, *12*, 593–601.
- (62) Tahir, A. A.; Wijayantha, K. G. U.; Yarahmadi, S. S.; Mazhar, M.; McKee, V. *Chem. Mater.* **2009**, *21*, 3763–3772.
- (63) Shinde, P. S.; Go, G. H.; Lee, W. J. *J. Mater. Chem.* **2012**, *22*, 10469–10471.
- (64) González-Borrero, P. P.; Sato, F.; Medina, A. N.; Baesso, M. L.; Bento, A. C.; Baldissera, G.; Persson, C.; Niklasson, G. A.; Granqvist, C. G.; Ferreira da Silva, A. *Appl. Phys. Lett.* **2010**, *96*, 061909.
- (65) Johansson, M. B.; Baldissera, G.; Valyukh, I.; Persson, C.; Arwin, H.; Niklasson, G. A.; Österlund, L. *J. Phys.: Condens. Matter* **2013**, *25*, 205502.
- (66) Granqvist, C. G. *Handbook of Inorganic Electrochromic Materials*; Elsevier Science, Amsterdam, The Netherlands, 1995.
- (67) Lee, J. S.; Kim, J. H.; Lee, Y. J.; Jeong, N. C.; Yoon, K. B. *Angew. Chem., Int. Ed.* **2007**, *46*, 3087–3090.
- (68) Khanh, N. N.; Yoon, K. B. *J. Am. Chem. Soc.* **2009**, *131*, 14228–14230.
- (69) Pham, T. C. T.; Kim, H. S.; Yoon, K. B. *Science* **2011**, *334*, 1553–1558.
- (70) Vidyarthi, V. S.; Hofmann, M.; Savan, A.; Sliozberg, K.; König, D.; Beranek, R.; Schuhmann, W.; Ludwig, A. *Int. J. Hydrogen Energy* **2011**, *36*, 4724–4731.
- (71) Su, J. Z.; Feng, X. J.; Sloppy, J. D.; Guo, L. J.; Grimes, C. A. *Nano Lett.* **2011**, *11*, 203–208.
- (72) Kim, H. S.; Jeong, N. C.; Yoon, K. B. *Langmuir* **2011**, *27*, 14678–14688.